Zero-Aberration, Actinic, EUV Mask Inspection Microscope with High Defect Sensitivity

Kenneth C. Johnson kjinnovation@earthlink.net 1/25/2015

Abstract

This paper describes an EUV spot-scanning microscope, which performs actinic, through-pellicle photomask inspection for EUV lithography. A primary benefit of spot-scanning microscopy is that it provides access to each illuminated spot's angular reflectance spectrum, which is sensitive to pure-phase mask defects. Additionally, the spot generation and detection optics can entirely nullify geometric aberrations in the imaging system, potentially resulting in simplified, lower-cost and higher-performing imaging optics.

1. Introduction

A spot-scanning EUV mask inspection system operates by raster-scanning a photomask across an array of discrete, diffraction-limited EUV focus spots and detecting the reflected radiation from each spot to synthesize a full-field EUV image of the mask. Two primary advantages of this system are:

(1) It can detect symmetry imbalances in each illuminated spot's angular reflectance spectrum, providing robust sensitivity to pure-phase, as well as pure-amplitude, mask defects; and it can clearly distinguish between phase and amplitude defects.

(2) The spot-generation optics (EUV microlenses) can be configured to produce diffraction-limited spots on the mask with zero geometric aberration, and can be achromatized to operate with a commercial, broadband EUV source such as the Adlyte LPP (laser-produced plasma) system (http://www.adlyte.com/).

These capabilities are discussed in sections 2 and 3, after which system design and performance characteristics will be discussed in section 4. (The focus of this paper is EUV microscopy, but the same principles are applicable to DUV or visible microscopy.)

2. Phase defect detection

Consider a conventional, full-field-illumination microscope, which detects small defects on an unpatterned (blank) background. The electromagnetic field's complex amplitude on a particular detector pixel is normalized to 1 for a blank image (no defect), resulting in unit field intensity $I = 1$. In the presence of a small (sub-resolution) defect the amplitude is perturbed by a small increment a, resulting in a field intensity of

$$I = |1 + a|^2 = 1 + 2\,\mathrm{Re}[a] + |a|^2$$

The $|a|^2$ term is typically below the detection threshold, leaving the $\mathrm{Re}[a]$ term as the only indicator of the defect's presence. Defect visibility is good for a pure-amplitude defect (i.e., real-valued a), but a pure-phase defect (i.e., pure-imaginary a) is invisible to the microscope.

The defect-scattered light is concentrated mainly in the field's high spatial frequencies, which can be phase-shifted relative to low frequencies to enhance defect visibility. The phase shift can be effected either by designing an annular phase retarder into the system pupil (by the method of Zernike phase-contrast microscopy), or by defocusing the image. For example, if a $\pi / 2$ phase shift is applied to the defect amplitude a, then the resulting field intensity becomes

$$I = |1 + i\,a\,|^2 = 1 - 2\,\mathrm{Im}[a] + |\,a\,|^2$$

In this case, the system exhibits high sensitivity to a pure-phase defect, but is insensitive to a pure-amplitude defect. For any particular complex amplitude a, the phase shift can be selected to provide optimum defect sensitivity; but it is not possible to choose the phase shift to provide good sensitivity for all defects. Thus, multiple images would need to be acquired with different phase shifters, or different focus offsets, to ensure visibility of all detectable defects.

A spot-scanning microscope, by contrast, can exhibit good sensitivity for both phase and amplitude defects simultaneously by detecting the far-field angular intensity distribution from each illumination spot. Figure 1 shows a (greatly simplified) conceptual schematic of the system. For clarity of illustration the object (photomask) is represented as a transmission element. Illumination is focused onto a diffraction-limited spot on the object, and is sensed by a detector element covering the transmitted beam's full angular range. (Each point P on the detector receives radiation directed at a corresponding ray angle θ from the beam axis in Figure 1.) A single detector element integrating over the full angular range would be sensitive to pure-amplitude defects, but insensitive to pure-phase defects, as described above. However, a pure-phase defect will induce an imbalance in the intensity distribution across the detector surface, which can be sensed by partitioning the detector into multiple sensor elements.

A numerical example, based on a Fourier-optics simulation, illustrates the effect. The simulation wavelength is 13.5 nm, and the scan point is at the focus of a coherent beam of NA (numerical aperture) 0.16. The defect is a disk of diameter 10 nm, within which the object transmittance is $1 + a$ (relative to a defect-free background transmittance of 1). Two cases will be considered: $a = -0.1$ (pure amplitude) and $a = 0.1i$ (pure phase). The complex field amplitude across the detector is approximated as the Fourier transform of the object field amplitude, which is a realistic approximation when the object-to-detector distance is much larger than the focus spot.

The illumination spot is characterized by an amplitude point-spread function PSF, which remains stationary as the object surface is scanned across the spot; see Figure 2. A small defect on the object affects the detector's intensity profile, which varies dynamically as the defect scans the spot. For this simulation the defect scans through the illumination beam axis, and the defect displacement from the spot center is denoted x (which varies linearly with time). Figure 3a illustrates calculated cross-sectional intensity profiles over the detector in the plane of Figure 2 at several defect positions x, for case 1 ($a = -0.1$), and Figure 3b shows similar profiles for case 2 ($a = 0.1i$). The horizontal axis coordinate ($\sin\theta$) in Figures 3a and 3b is related to the ray angle θ in Figure 1.

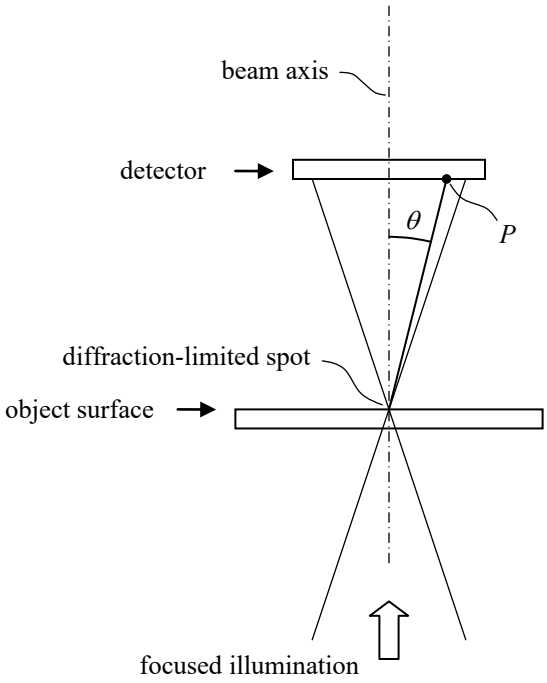

Figure 1. Simplified spot-scanning microscope schematic.

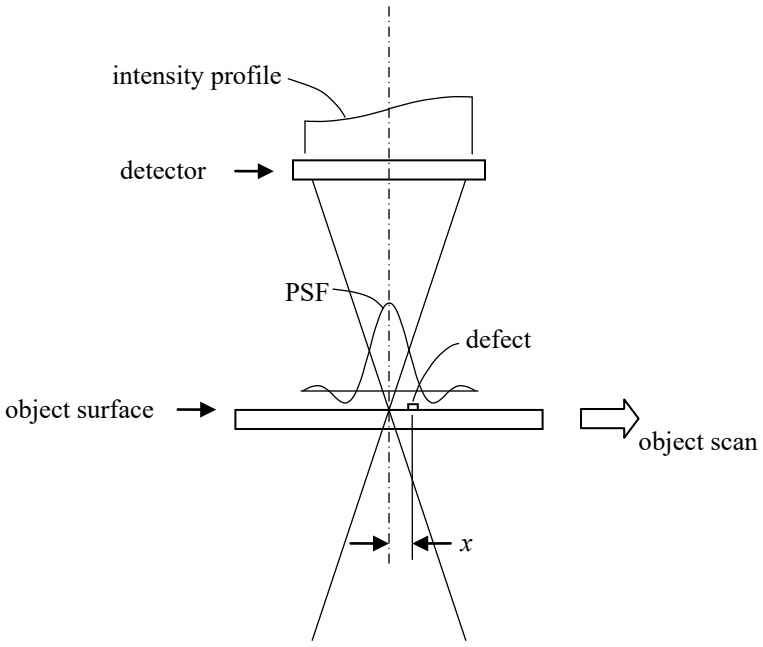

Figure 2. Defect detection.

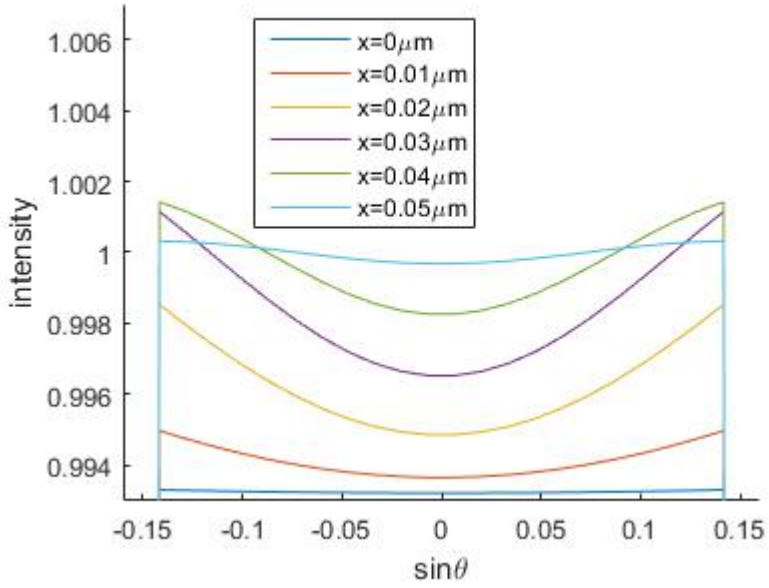

Figure 3a. Detector intensity profile for case 1 ($a = -0.1$).

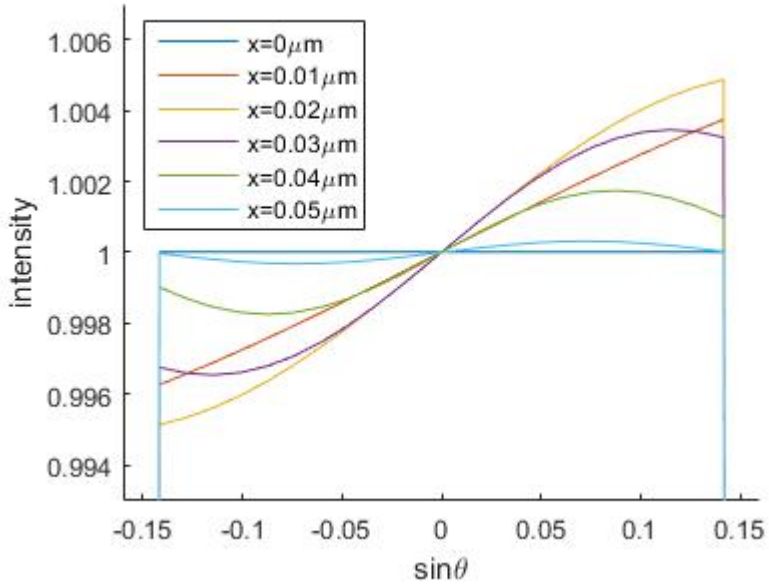

Figure 3b. Detector intensity profile for case 2 ($a = 0.1i$).

A full area-integrating detector can sense the signal variations illustrated in Figure 3a, but a partitioned detector is needed to detect changes in the intensity distribution as shown in Figure 3b. For example, the detector can comprise four quadrant sensors centered on the beam axis, as illustrated in Figure 4. The area-integrated sensor signals over the four quadrants are indicated as I_1, I_2, I_3, and I_4, and the following derived signals are determined from these quantities (either digitally or via analog electronics):

$$I = I_1 + I_2 + I_3 + I_4$$
$$I_x = I_1 - I_2 - I_3 + I_4$$
$$I_y = I_1 + I_2 - I_3 - I_4$$

I is the total integrated signal. I_x and I_y are components of a vector representing the intensity gradient over the detector. For a defect-free object $I = 1$, $I_x = 0$, and $I_y = 0$ over the full x scan. Figures 5a and 5b show plots of $I - 1$, I_x, and I_y for the two cases described above. The combination of I, I_x and I_y scans provides robust detection capability for both pure-amplitude and pure-phase defects.

I_y is identically zero in Figures 5a and 5b. The plots represent a single line scan with the defect traversing the beam axis, but with a full, two-dimensional raster scan both I_x and I_y will provide useful information on phase defects. In practice, the object can be continuously scanned across a large array of illumination spots, as illustrated in Figure 6, to cover a large area with multiple interleaved line scans.

Two advantages of this method for inspecting phase defects are that (1) the subtraction operations used to calculate I_x and I_y will tend to eliminate common-mode noise or systematic errors in the signals, and (2) the defect locations are precisely determined by the zero crossings of I_x and I_y.

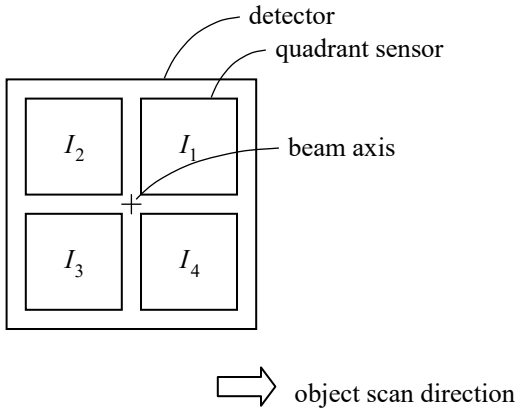

Figure 4. Quadrant detector.

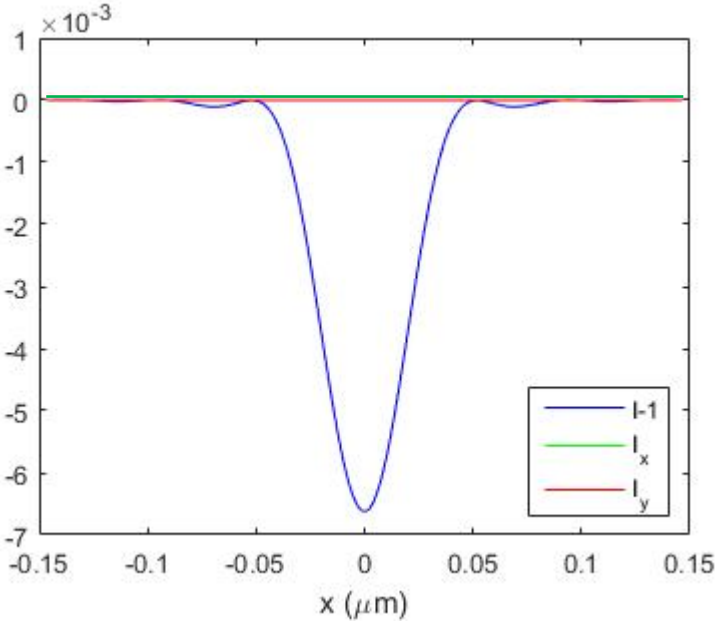

Figure 5a. Line scan plots for case 1 ($a = -0.1$).

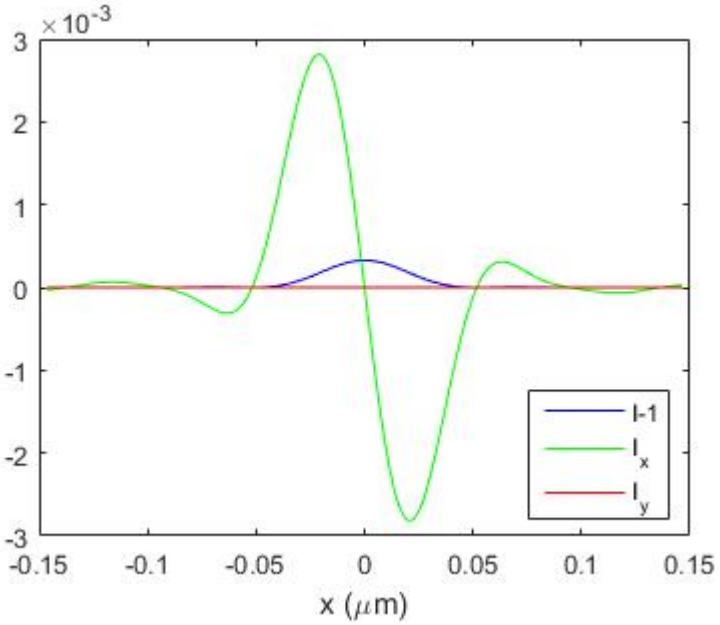

Figure 5b. Line scan plots for case 2 ($a = 0.1i$).

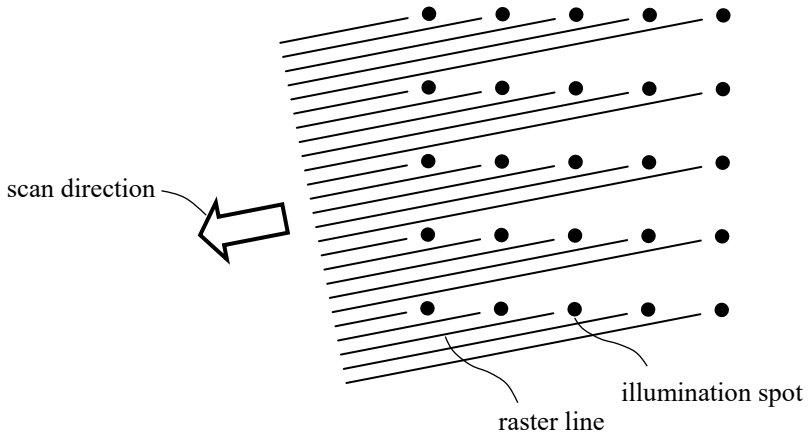

Figure 6. Raster scan pattern on mask (interleaved line scans).

The above description is applicable to detection of isolated defects on an unpatterned sample, but the system can also be used for pattern inspection or metrology. The system can image patterns using a variation of coherent diffraction imaging (CDI) and ptychography.[1, 2, 3] But in the Figure-1 schematic the illumination has a much wider numerical aperture (NA), and is focused to a much smaller spot, than what is typically used for CDI. As a consequence of the higher illumination NA (comparable to the detector's collection NA), image resolution is improved. Also, the very small, diffraction-limited illumination spot generates a diffraction pattern that has minimal spatial variation, so very few detector elements are needed for each illumination spot. For example, the quadrant detector (Figure 4) has only four elements, whereas CDI systems more typically use detector arrays with thousand or millions of elements. Image reconstruction algorithms would be simplified by the very small illumination spot and the relatively small number of detector elements.

Multiple spots are illuminated in parallel, as illustrated in Figure 6, to achieve high-throughput imaging. But the total instantaneous field area covered by the spots is a small fraction of the full scan area, so even with parallel-spot scanning the total number of detector elements would be modest. Due to the high power concentration at the illumination spots, the power flux levels on the detector array would be comparatively high, but the detector readout rate would also need to be comparatively high to achieve good imaging throughput relative to a conventional CDI system with full-field illumination. Thus, the system described herein would require relatively few detector elements operating at a relatively high readout rate.

---

[1] Thibault, Pierre, et al. "High-resolution scanning x-ray diffraction microscopy." *Science* 321.5887 (2008): 379-382. http://dx.doi.org/10.1126/science.1158573

[2] Zhang, Bosheng, et al. "Quantitative tabletop coherent diffraction imaging microscope for EUV lithography mask inspection." *SPIE Advanced Lithography*. International Society for Optics and Photonics, 2014. http://dx.doi.org/10.1117/12.2046526

[3] Karl, Robert, et al. "Spatial, spectral, and polarization multiplexed ptychography." *Optics express* 23.23 (2015): 30250-30258. http://dx.doi.org/10.1364/OE.23.030250

3. Spot generation and detection optics

The system concept illustrated in Figure 1 is over-simplified, but Figure 7 shows a more realistic, although still idealized, schematic of a spot-scanning microscope. Illumination is directed through spot-generation optics comprising a microlens array, which condenses the radiation onto an array of focal spots. The spots are imaged onto the object surface by illumination optics and are then reimaged by collection optics. (As illustrated, the illumination optics and collection optics are both double-telecentric.)

The detector elements in Figure 7 are not located proximate the object as in Figure 1; instead the object is imaged by collection optics onto a conjugate image plane and the detector elements are proximate the image plane. (The detector cannot be right at the image plane; it must be displaced some distance from the image plane to provide adequate resolution of the angular intensity spectrum from each spot.) This arrangement provides for a long working distance between the object and adjacent optics, which is necessary for through-pellicle viewing with reflective optics. In an EUV inspection system the object (mask) and all of the large lenses in Figure 7 would be replaced by reflective elements.

The microlenses are EUV-transmitting elements. EUV optical materials have poor transmission efficiency, except in very thin sections, but this limitation is overcome by structuring the EUV microlenses as phase-Fresnel diffracting elements. Diffractive lenses exhibit high chromatic dispersion, which would be problematic if a broadband source such as the Adlyte LPP is used. But this problem can be overcome by designing each microlens as Schupmann doublet[4], which combines a converging element and a diverging element in a configuration that is achromatic over the LPP's 2% wavelength band.

Figure 8 shows a schematic cross-section of the microlens array. (Three Schupmann doublets and corresponding edge rays are illustrated.) Each doublet comprises a positive-power (converging) element **L1** followed by a negative-power (diverging) element **L2**, with an intermediate lens focus formed between the two elements. (The converging element **L1** is concave, and the diverging element **L2** is convex, because the lens material's refractive index is less than 1 at EUV wavelengths.) The virtual foci behind the diverging elements are imaged onto the object surface.

L1 and **L2** are both phase-Fresnel molybdenum structures formed on thin silicon substrates, and they are supported by a hollow microchannel plate. The phase-Fresnel form can be approximated by a multilevel staircase profile, as illustrated by the enlarged detail view in Figure 8. The lenses can be fabricated by applying several overlaid deposition/etch processes (using thin ruthenium layers as an etch stop between the

[4] U.S. Patent 9,097,983

molybdenum layers). A similar process is used for EUV phase-shift masks[5]. The silicon substrate layers can be thinner than EUV pellicles because structural support is provided by the microchannel plate.

Typical design dimensions would be, e.g., 20-micron lens diameter and 1-mm microchannel thickness. (This results in 0.04-NA beam divergence at the virtual foci, and with 4X demagnification the NA at the object surface would be 0.16.) Each lens would have eight Fresnel facets, with each facet comprising four or eight staircase levels. The minimum facet width is 0.7 micron, and the facet heights are 0.18 micron. Depth tolerances would be comparatively loose in relation to EUV mask layers because transmission optics are generally less sensitive to surface profile errors than reflective optics (especially with the very low refractive index contrast of molybdenum). With 4X demagnification, lateral tolerances on the phase-Fresnel structures would be expected to be about 4 times looser than EUV photomasks.

The doublet's EUV transmission efficiency at wavelength 13.5 nm is approximately 36% neglecting substrate losses and microchannel fill-factor losses.

Each microlens doublet is designed to transform a source-generated optical wavefront (from the LPP source's center point) into a perfectly spherical wave converging to a point on the object surface after the wave traverses the illumination optics. Geometric aberrations in the illumination optics are nullified by the microlenses. A single microlens has sufficient design degrees of freedom to achieve perfect point-to-point imaging free of geometric aberration at one design wavelength, and two microlenses in a Schupmann configuration have sufficient degrees of freedom to achieve perfect point imaging at two wavelengths. With the LPP source's 2% wavelength band and the microlenses' small dimensional scale, two-wavelength correction suffices to effectively eliminate chromatic aberration in the illumination system.

The detector optics may include a couple of optional mechanisms illustrated in the enlarged detail view in Figure 7. An aberration corrector such as a molybdenum layer of nonuniform thickness on a silicon membrane can correct aberrations in the collection optics. The collection optics do not need to have good point-imaging performance, but the corrector plate can operate to provide uniform, caustic-free illumination over the detector elements, and can help to preserve the symmetry properties of the intensity profiles illustrated in Figures 3a and 3b. (Odd-parity aberrations such as coma could distort the profiles asymmetrically and change the intensity balance between pixel quadrants.) It may also be advantageous to use a small field lens at the conjugate focal point to image the system pupil onto the pixel aperture. (The aberration corrector and field lens are not achromatized, but chromatic effects would be insignificant because they have very low optical power.)

---

[5] Jung, H. Y., et al. "Selective dry etching of attenuated phase-shift mask materials for extreme ultraviolet lithography using inductively coupled plasmas." *Journal of Vacuum Science & Technology B* 27.6 (2009): 2361-2365. http://hint.skku.edu/master/pds_notice/Download/HINT_20100202050216.pdf

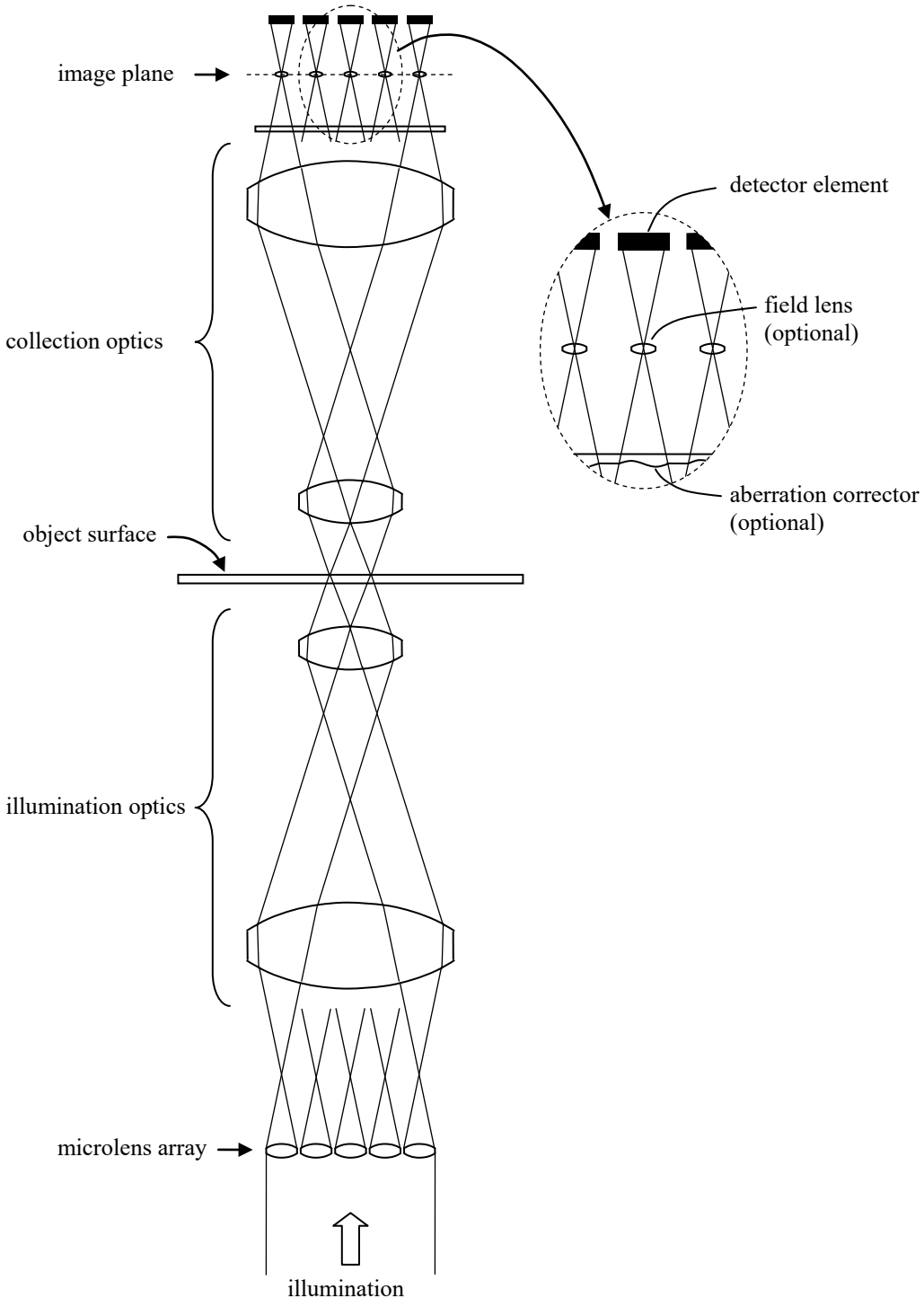

Figure 7. Spot-scanning microscope schematic.

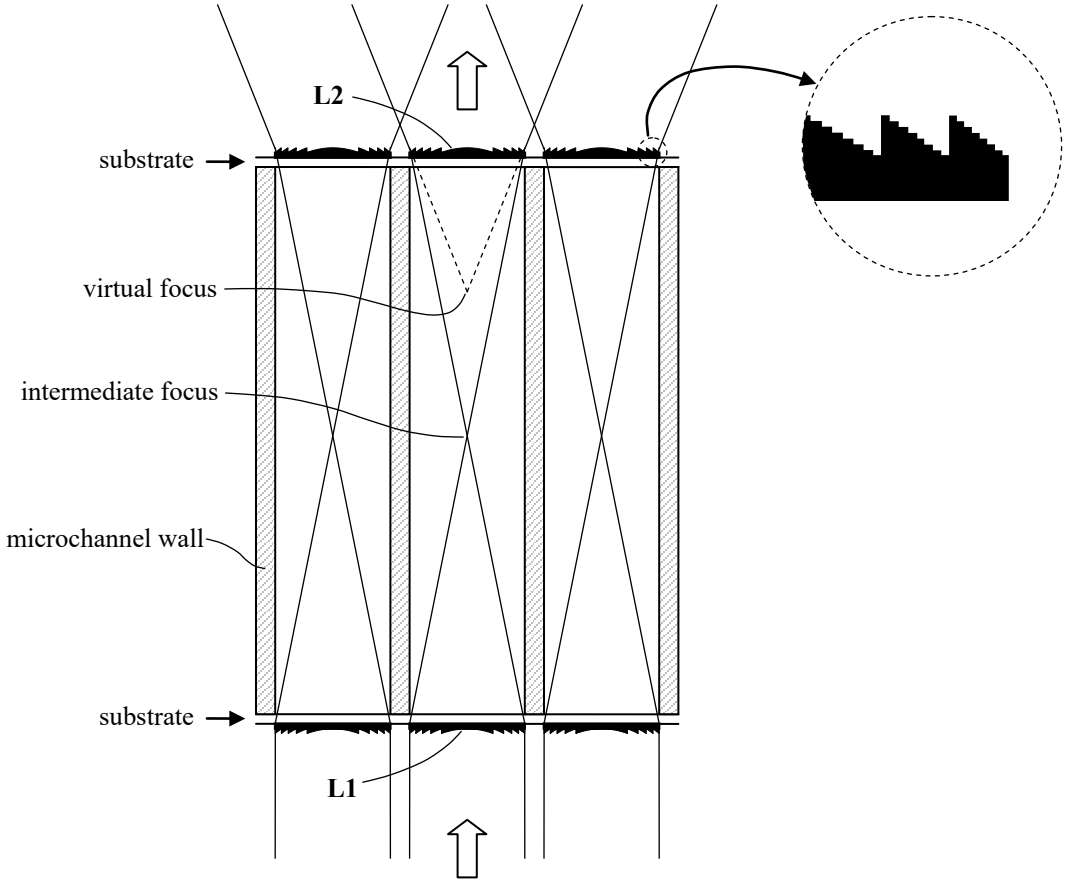

Figure 8. Microlens array schematic.

4. System design

The illumination and collection optics shown schematically in Figure 7 could be designed as catoptric systems similar to EUV lithography scanners, but with two significant simplifications: First, the NA would be much lower, e.g. 0.16 or lower at the mask[6], versus a lithography scanner's NA of 0.33 at the wafer. Second, the micro-optics' aberration-correcting capability could significantly simplify the optical design.

Some system design and performance parameters can be estimated or bounded based on general physical constraints, without reference to an actual optical design. One such constraint is the diffraction limit. If the LPP were an ideal point source the focus spots would have the form of Airy disks (assuming a circular illumination pupil). The first Airy ring has a radius of $0.61\lambda / NA$ (e.g. approximately 50 nm with $\lambda = 13.5\,\text{nm}$ and $NA = 0.16$). The geometric image size of the actual LPP source should be comparable to or smaller than this dimension to avoid significant loss of image resolution.

[6] KLA-Tencor's EUV inspection system (the Teron 700 series, now discontinued) was designed for NA = 0.16. http://www.sematech.org/meetings/archives/litho/euvl/10157EUVL/pres/KT%20Wack.pdf

In general the geometric etendu of each focus spot should be of order λ^2 (or lower) to preserve diffraction-limited imaging, and the collected source etendu divided by this value provides an estimate of the minimum required number of microlenses. The Adlyte LPP source radius is at least 25 microns, and the collection solid angle is approximately 0.2 steradian.[7] (The angle can be higher, but at considerably increased cost.) This implies a collected source etendu of $\pi(25\,\mu\text{m})^2(0.2\,\text{Sr})$, and dividing this number by λ^2 yields the estimated number of microlenses and associated detector pixels: $2\cdot10^6$.

Due to the sparse illumination pattern the required number of pixels is much less than what would be needed for conventional microscopy with full-field illumination. (On the other hand, the EUV power and data readout rate per pixel are much higher.) Also, each "pixel" would probably be a quadrant sensor (Figure 4), so the total number of sensor elements would be $8\cdot10^6$.

Assume a mask illumination field of $50\,\text{mm}^2$ for inspection. (This is comparable to the wafer-plane ring field area of an EUV lithography scanner.) With 4X-reduction illumination optics, the approximate microlens diameter is $4\sqrt{50\,\text{mm}^2/(2\cdot10^6)} = 20\,\mu\text{m}$. Using 4X-magnification collection optics between the mask and detector, the detector pixel size would also be of order $20\,\mu\text{m}$ (or $10\,\mu\text{m}$ per quadrant).

With a raster step size of 10 nm, the number of image frames required to cover a $(141\,\text{mm})^2$ mask area would be $(141\,\text{mm})^2/(10\,\text{nm})^2/(2\cdot10^6) = 10^8$. The Adlyte source repetition rate is 10 kHz (although it could probably be increased to 20 kHz), implying a mask scan time of $10^8/(10^4\,\text{sec}^{-1}) = 10^4\,\text{sec}$ (i.e., approximately 3 hours). The detector frame rate is assumed to be matched to the 10 kHz source rep rate.

The Adlyte source brightness is $1000\,\text{W}/(\text{mm}^2\,\text{Sr})$ at intermediate focus.[8] Assuming 1% radiance transmittance from the intermediate focus to the detector, the brightness at the detector would be $10\,\text{W}/(\text{mm}^2\,\text{Sr})$. This value is multiplied by the geometric etendu per spot, λ^2, to get the average power per pixel: $(10\,\text{W}/(\text{mm}^2\,\text{Sr}))((13.5\,\text{nm})^2\,\text{Sr}) = 1.8\cdot10^{-9}\,\text{W}$. At the 10 kHz pulse repetition rate the collected energy per pixel per pulse is $((1.8\cdot10^{-9}\,\text{J/sec})/(10^4\,\text{sec}^{-1}))(6.24\cdot10^{18}\,\text{eV/J}) = 1.1\cdot10^6\,\text{eV}$. At $92\,\text{eV}$ per EUV photon, this equates to 12,000 photons. With quadrant

[7] The Adlyte system parameters used in this analysis are based on information on the Adlyte website (http://www.adlyte.com/) and personal communication with Dr. Reza Abhari of ETH Zürich (http://www.lec.ethz.ch/people/staff_phd/abhari).

[8] This significantly exceeds the $20\,\text{W}/(\text{mm}^2\,\text{Sr})$ of KLA-Tencor's system. http://www.euvlitho.com/2014/S93.pdf

sensors, the photon count would be 3000 per quadrant. (By comparison, the required number of photons reported in the literature[9] is 1400.)

[9] Wintz, Daniel T., et al. "Photon flux requirements for EUV reticle imaging microscopy in the 22-and 16nm nodes." SPIE Advanced Lithography. International Society for Optics and Photonics, 2010. http://goldberg.lbl.gov/papers/Wintz_SPIE7636_2010.pdf